Applied Surface Science 546 (2021) 149050

Contents lists available at ScienceDirect

Applied Surface Science

journal homepage: www.elsevier.com/locate/apsusc

Full Length Article

Glass surface micromachining with simultaneous nanomaterial deposition by picosecond laser for wettability control

Zhen Wang, Dhiraj Nandyala, Carlos E. Colosqui, Thomas Cubaud, David J. Hwang *

Department of Mechanical Engineering, State University of New York, Stony Brook, NY 11794, USA

ARTICLE INFO

Keywords:
Ultrafast laser
Glass micromachining
Pulsed laser deposition
Multi-hierarchical micro/nanostructures
Contact angle hysteresis
Liquid infused surfaces

ABSTRACT

Glass surface micromachining with simultaneous redeposition of nanomaterials in the vicinity of machined microscale trenches is achieved using a picosecond laser of visible wavelength in ambient air. After investigating the spatial distribution of redeposited nanomaterials by a unit discrete laser micromachining line, multi-line patterns machined with variable interline separations are characterized using optical and scanning electron microscopes. For large interline separations, laser machined debris was redeposited in the form of web-like nanofibrous aggregates with significant spatial variation in density. Reduced separations improved spatial uniformity but the increased material density induced noticeable conversion from web-like nanofibrous to fractal-like nano-cauliflower structures. In this way, picosecond laser machining processes enabled a single-step fabrication of multi-hierarchical micro/nanostructures on arbitrary glass surface areas with tunable nanomaterial structures. Based on the wetting behavior on patterned surfaces in ambient air by using the patterned surfaces as Wilhelmy plates in force-displacement measurements and *in-situ* optical microscope inspection, we find that contact angle hysteresis is suppressed for surfaces patterned with sufficiently small line separations due to the water infusion in the deposited nanomaterials. The studied laser processing method can be potentially employed for fast and effective fabrication of liquid infused surfaces with complex microscale patterns combined with controllable nanofeatures.

1. Introduction

Control of liquid wetting behavior on a solid surface by tuning its micro/nanoscale surface morphology has been an active research theme, enabling a wide range of applications [1–3]. Glass has been widely used in fluidic or optofluidic applications due to its intrinsic hydrophilicity and optical transparency as well as its thermal, chemical, and mechanical stability, and suppressed optical and spectroscopic noise [4–7]. However, glass surface micromachining is not a minor task by the conventional means due to the brittle nature of glass materials with high risk of unwanted crack generation. While the intrinsic hydrophilicity of glass surfaces is advantageous for diverse microfluidic applications, its wetting behavior can be further altered by extra surface patterning in micro/nano scales to enable a wider range of applications [8–10].

Laser based surface patterning techniques, categorized as a non-contact machining method, have been particularly useful for glass materials, offering mask-less single-step processing capabilities. High-precision and high-efficiency glass surface micropatterning has been enabled by short pulsed lasers of ultraviolet wavelength [11], but more recently ultrashort (i.e., picosecond or femtosecond) pulsed lasers have shown a great promise in high-precision glass machining with the minimized heat affected zone, and the practically convenient visible to near-infrared wavelengths can be also used via the nonlinear absorption process [12–14].

Nanofeatures are typically accomplished through a secondary step either by transferring pre-synthesized nanomaterials to [10,15] or by synthesizing nanomaterials on a pre-fabricated microstructure [16]. Laser ablation has been exploited to convert bulk materials into various types of nanomaterials. However, nanomaterials have been mostly collected in the form of dry powders or dispersed in liquid for subsequent transfer processes [17–19]. Direct deposition of laser ablation produced nanomaterials has been also attempted in pulse laser deposition (PLD) configurations [20], but vacuum control is necessary to ensure the arrival of ablated species and difficulties in achieving spatial uniformity over a large sample area limit its practicality.

It is interesting to note that the ablative laser surface micromachining process has shown a unique potential to the simultaneous incorporation of nanofeatures on or near the machined microfeatures

* Corresponding author.
E-mail address: david.hwang@stonybrook.edu (D.J. Hwang).

https://doi.org/10.1016/j.apsusc.2021.149050
Received 27 August 2020; Received in revised form 16 December 2020; Accepted 12 January 2021
Available online 16 January 2021

[21–23]. The source of nanomaterials is redeposition of laser-ablated material plume in an ambient gaseous environment. Rapidly expanding material ejecta in vapor or plasma phase (typically at the velocity order of 10^3-10^5 m/s, depending on laser pulse energy and temporal pulse width) strongly compress the ambient gas forming a shock, and under this situation the subsequent material ejecta tends to be bounced back and redeposited onto the sample surface triggered by high recoil pressure in the form of rarefaction wave. In this course, nanomaterials are formed through the collision assisted agglomeration of condensed species and nucleation based growth within the ablation plume. The resulting multi-hierarchical micro/nano structures demonstrated include super-hydrophilic surfaces [23–25] and superhydrophobic surfaces usually after an additional chemical coating step [22].

Although it appears that the arrangement of nanostructures is further tunable by adjusting laser ablation parameters, in particular, the spacing between laser processed regions, most of the demonstrated trends for achieving nanostructures were investigated in the course of random drilling or cutting process [26,27], thus not yet corresponding to the ultimate sample configuration of controlled micro/nano architectures by a single laser processing step. Overall, most of hybrid nanostructures were produced within laser-processed microstructures, and less attention has been paid to the nanostructures formed at the surrounding of laser processed region in a controllable fashion.

In this study, surface machining is performed on glass using picosecond laser of visible wavelength. The main focus of this research is in investigating the spatial distribution of redeposited nanomaterials in the surrounding region of machined trench. As the next step, multiple parallel line patterns at different interline separations are machined, followed by characterization of nanomaterials deposited in-between machined trenches. In this way, we attempt to cover with nanomaterials the entire sample area towards a single-step fabrication of multi-hierarchical micro/nano structures on glass surfaces of arbitrary area. The role of interline separation on wetting behavior is also examined in conjunction with the structure and distribution of deposited nanomaterials.

2. Experimental procedure

Borosilicate glass was selected as a base material. A picosecond laser of 532 nm in wavelength, ~12 ps in full width half maximum temporal pulse width, 100 kHz in the pulse repetition frequency and up to 7 W in average laser power, was utilized for this study. A schematic diagram of laser surface micromachining setup is shown in Fig. 1(a). Laser beam was focused on the glass surface with an infinity-corrected objective lens of 0.14 in numerical aperture to the laser focal spot diameter of ~10 μm ($1/e$ definition), as experimentally measured by Gaussian fitting process based on features generated by various laser power levels [28]. Laser power was precisely adjusted by an external attenuator set composed of a half waveplate and a polarizing beam splitter. A zoom lens and a charge-coupled device (CCD) camera were implemented at the back of the objective lens to precisely locate laser focus on the sample surface and *in-situ* monitor the laser machining process. Glass sample was scanned with a fixed speed of 20 mm/s and a fixed laser power of 400 mW for both a single discrete line type and multi-line surface machining processes. For multi-line machining process (Fig. 1(b)), the spacing between line centers was adjusted to 25, 50, 100 and 200 μm, respectively, and line patterns were fabricated on both sides of glass. After laser machining process, the processed glass sample was cleaned by injecting deionized water to remove loosely mounted ablation species off from the sample surface, and was subsequently blown with extra dry nitrogen gas. Laser patterned samples were also etched in HF solution (buffered oxide etchant of 10 H_2O : 1 HF concentration, 30 min etching time with intermittent shaking of the etching apparatus) to remove loose components including machined debris [29,30] and thus only leaving micro-machined trenches as reference samples regardless of laser processing conditions. Optical microscope (F70, Mitutoyo) and scanning electron microscope (SEM, JEOL 7600F) after Au/Pd sputtering were used for morphological analysis of the machined features.

The contact angle for the patterned surfaces by water in ambient air and its static hysteresis was measured with the Wilhelmy plate method under "quasi-static" conditions for which hydrodynamic friction is negligible. Optical microscope imaging was also utilized to investigate the detailed microscopic wetting behavior depending on the interline separations and characteristics of nanofeatures in-between line patterns.

It is mentioned that all the optical and scanning electron microscope images and all the Wilhelmy plate measurements of the laser processed samples before HF etching were taken after the aforementioned cleaning steps composed of the mild water injection and nitrogen gas blowing.

3. Results and discussion

3.1. Characteristics of a single discrete machining line

Characteristics of a single discrete laser machining line are first examined as a baseline to understand the subsequent multi-line steps, and results by the laser power of 400 mW and scanning speed of 20 mm/s are summarized in Figs. 2 and 3. 400 mW was the laser power that exceeds ablation threshold and generate micro-trenches of approximately 10 μm machined width. The single discrete machining line was selected from multi-line patterns with a interline separation of 200 μm, considering the existence of a wide range of unaffected zone between machined lines.

Top view and cross-sectional SEM images in Fig. 2(a) show detailed morphology of machined trench; ~10.6 μm in width and ~ 7.7 μm in depth at given laser machining conditions. A few different types of machined debris are visible - multiple fragments of a few micron size are found in the vicinity of machined trench, and the machined region and its surroundings are covered with fine sized debris. As shown in Fig. 2

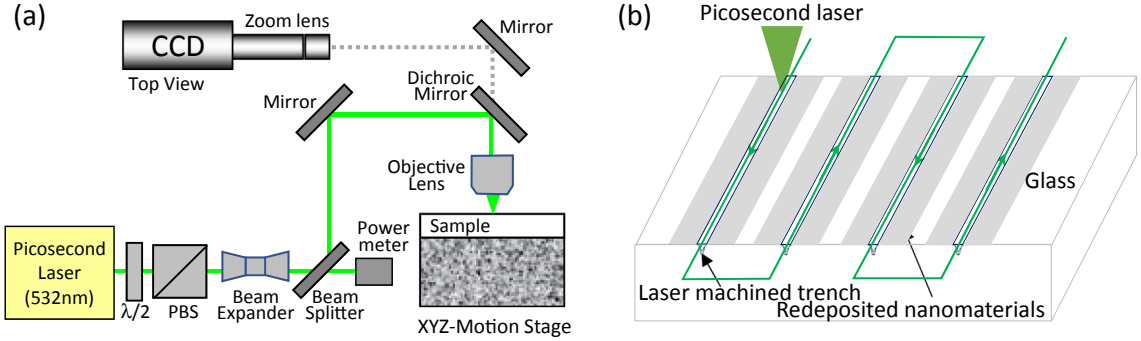

Fig. 1. Picosecond laser based glass surface micromachining procedures. (a) Laser machining set up, and (b) surface patterning and simultaneous nanomaterial deposition by laser micromachining process.

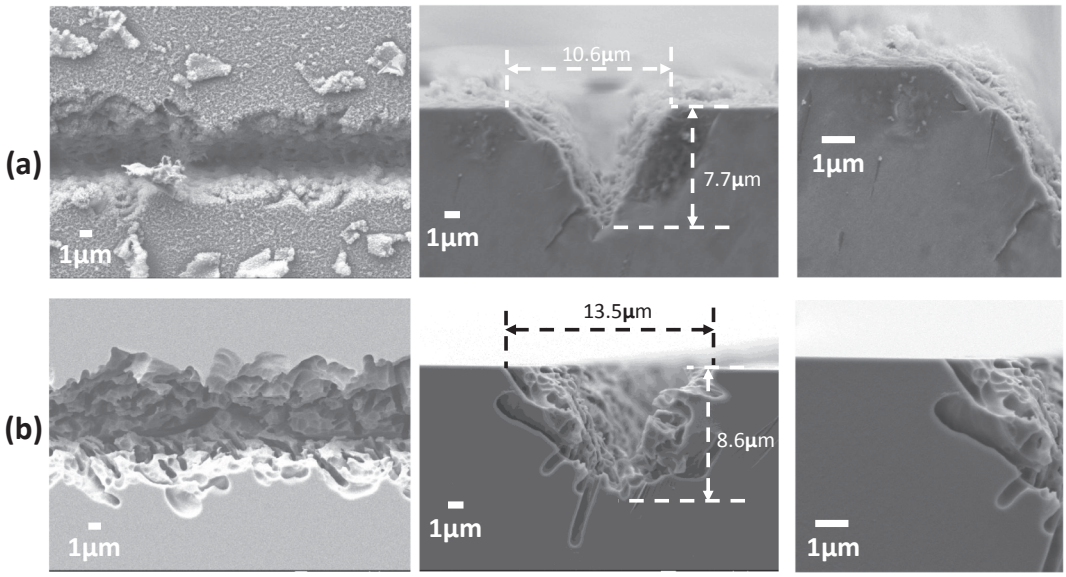

Fig. 2. Laser based glass surface micromachining results by a single discrete line scanning. A picosecond laser beam of ~12 ps in temporal pulse width, 532 nm in wavelength, 100 kHz in pulse frequency and 400 mW in average power was focused on the glass sample surface at ~10 μm focal spot diameter, and sample was scanned at 20 mm/s. (a) Scanning electron microscope (SEM) images of laser machined trench; top view (left), and cross-sectional view (center) with its further zoom-in (right), and (b) SEM images of laser machined trench after HF etching; top view (left), and cross-sectional view (center) with its further zoom-in (right).

(b), HF etching removed such loose debris, leaving micromachined trenches only with slightly increased width and depth of the trench. A clear trace of crack is inspected near the machined edge possibly caused by laser-induced shock as relatively high pulse energy was applied for the machining process. It is postulated that the micron-sized fragments seen in top view SEM image of Fig. 2(a) are induced features by such cracks.

For the identical machined trench, the overall affected zone is visualized by the zoomed-out optical microscope and SEM images in Fig. 3(a). The central dark region of ~10 μm width obviously corresponds to the laser-machined trench. It is noticed that the surrounding region exhibiting faint color is observed up to ~50 μm distance from laser machining center in both directions, representing the region where ablated materials are redeposited. The distance dependent characteristics of redeposited materials are inspected from a series zoomed-in SEM images in Fig. 3(b). While common characteristics are web-like nanofibrous structures composed of nanoparticles of ~20–30 nm (refer to Fig. 3(c)), the density of nanomaterials clearly varies depending on the distance from the machined center; dense networked nanofibrous structures are found at ~ 10–30 μm distance while the density of nanomaterials drops at ~40–60 μm distance. Nanomaterials of similar characteristics are also found within machined trench (Fig. 3(d)). A cross-sectional SEM image in comparison with SEM top view (Fig. 3(e)) further visualizes distance dependent distribution of redeposited nanomaterials from machined center as a material source for the surrounding redeposition. The lateral extent of redeposition should be closely related to that of the laser plume expansion under ambient air environment at a given laser machining condition.

Synthesis of such networked nanoparticle structures has been explained by the vapor condensation model [27,31]. Picosecond laser beam of visible wavelength is first absorbed in glass material, triggered by multi-photon absorption process and leading to optical breakdown state, followed by rapid expansion of material plume typically in plasma state. As the expansion process continues, the ablated species are cooled down into vapor and/or condensed into liquid phase, and subsequently nanoparticles grow via collision and nucleation process.

In the previous study on ultrafast laser based nanoparticles synthesis at room temperature in air, in the course of drilling arrays of micro-vias, around MHz was reported as threshold pulse frequency at which interweaving fibrous nanoparticle aggregates start to form by fusing nanoparticles within the timing of nanoparticle formation [26]. In this study, however, such fibrous nanoparticle networks were formed by picosecond laser of 100 kHz pulse frequency. Lower frequency does not necessarily mean that the extra laser pulse(s) induced fusion mechanisms are not available depending on the residence time of nanoparticles within the laser trajectory which is in turn dictated by laser ablation parameters. A relevant example is found from the previous work by authors; the aggregated networks composed of nanoparticles of ~20 nm size were collected by ablating a glass material with ultraviolet nanosecond laser of ~20 kHz pulse frequency focused to ~10 μm beam spot [19]. In fact, 10 μm laser beam spot is smaller than the lateral extent of plume expansion, and thus most of ablated species should escape out of incoming laser trajectory (three-dimensional expansion from a point-like source [32,33]) without being reheated by subsequent laser pulses. However, the ablation by 120 μm laser beam spot, which is closer to the extent of plume expansion, was subjected to one-dimensional plume expansion, and thus resulted in network structures composed of much larger particles of ~100 nm size caused by the active reheating by subsequent pulses. Similarly, the 100 kHz picosecond laser based ablation, in current study, is mostly free from reheating mechanism due to ~10 μm beam spot size, but web-like aggregation process was still efficient as rather a favorable trend in maintaining small unit particle size. As a mechanism responsible for the aggregation behavior in this study, it has been reported that the existence of background gas (vs. in vacuum) facilitates the aggregation of nanoparticles into web-like network structures [34]. As kinetic energy of ablation ejecta is significantly reduced by interaction with the background gas, the formation of web-like structure is attributed to the aggregation of nanoparticles suspended in the background gas for an extended period [35]. Repeated laser pulses in conjunction with a well-controlled spatial arrangement in this study, possibly aided the aggregation process through continuous supply of nanoparticles [26].

It is mentioned that large fragments of a few micron size are intermittently found mainly in the neighborhood of machined trench. It is likely that overlapping laser pulses of relatively high fluence frequently induced cracks in machining edge (remind such trend observed in Fig. 2) as a possible effect of laser induced thermal and/or shock, in contrast to the mechanism of large microparticle formation by ejection of molten

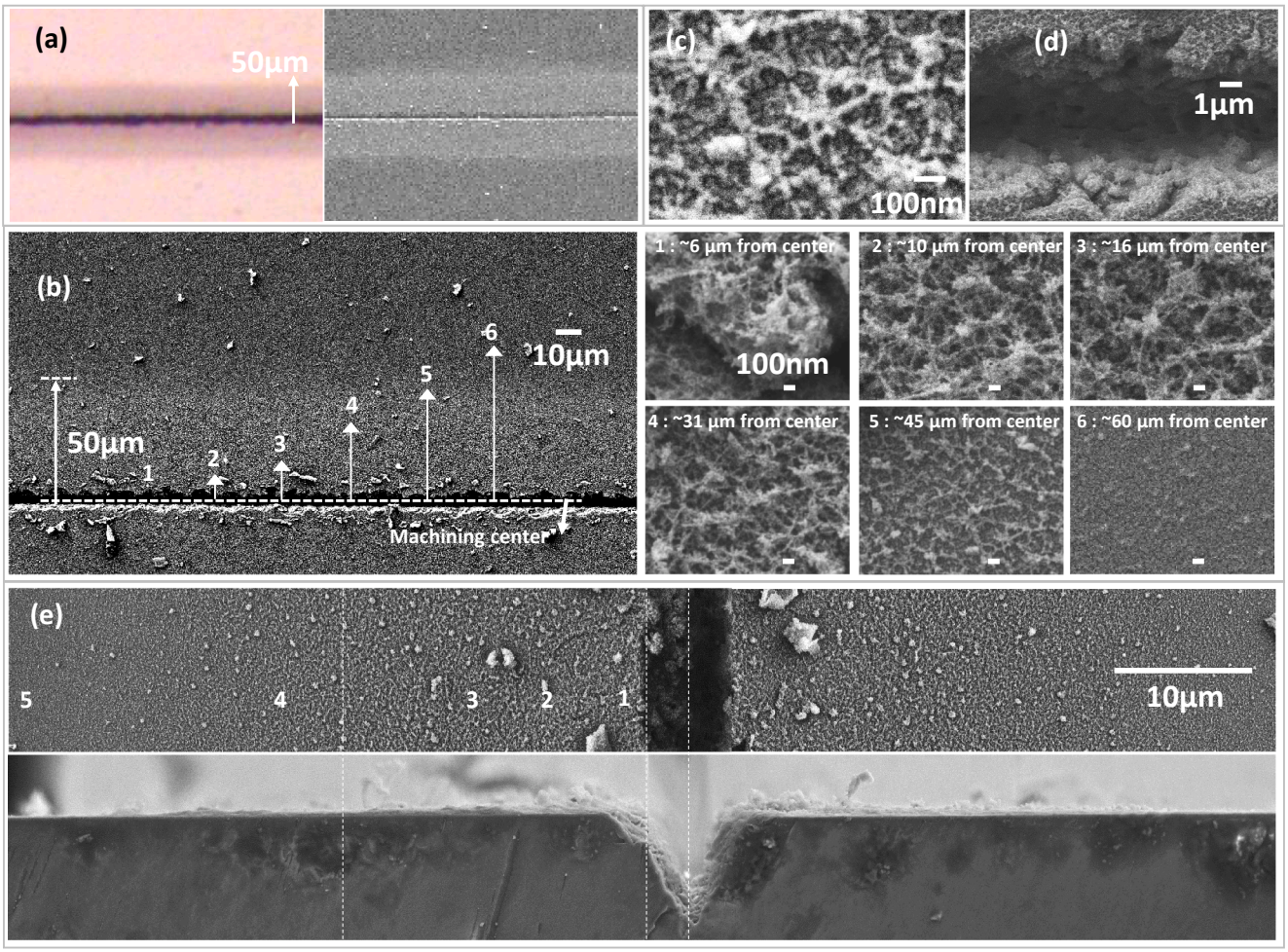

Fig. 3. Redeposition of machined debris by a single discrete line scanning of laser. A picosecond laser beam of ~12 ps in temporal pulse width, 532 nm in wavelength, 100 kHz in pulse frequency and 400 mW in average power was focused on the glass sample surface at ~10 μm focal spot diameter, and sample was scanned at 20 mm/s. (a) Optical microscope (left) and scanning electron microscope (SEM, right) images showing laser machining affected zone. (b) Zoomed-in SEM inspection of nanomaterials deposited depending on the distance from the machined center; indices of 1–6 indicate locations of different distances. (c) High magnification SEM image showing nanoparticle aggregates for the location 4 in (b). (d) A SEM image showing machined trench covered with redeposited nanomaterials. (e) A cross-sectional SEM image near machined crater (bottom) spatially matched with top view SEM image (top) showing spatial distribution of redeposited nanomaterials.

droplets in MHz regime [26]. The fragments could fly more than ~50 μm at a given laser machining condition (Fig. 3(b)). The morphology of fragments covered with nanofibrous structures (Fig. 2(a)) indicates that the fragments are first induced by the earlier laser pulse(s), and the nanomaterials are deposited by later laser pulse based ablation events.

3.2. Characteristics of multiple machining lines

The single line machining experiment in the previous section showed that the actual arrangement of redeposited nanomaterials is largely affected by the location specific supply of ablated materials. For the purpose of covering entire sample area with laser induced nanofeatures, multiple-line laser machining tests are performed with varied separations between neighboring machining lines. Laser machining parameters for unit line remain unchanged while variable interline separations of 200, 100, 50 and 25 μm are tested, as representative results are summarized in Fig. 4. In order to provide a guideline to the spatial distribution and overlapping effect upon multi-line laser processing, the lateral extents of machined trench (Machined width), Gaussian laser intensity profile for 10 μm beam diameter by $1/e$ definition (Laser intensity) and laser machining induced nanomaterials redeposition (Laser induced deposition zone) are schematically drawn on top portion of the figure. For each of interline separation, overall laser-machining affected zone is also visualized experimentally by optical microscope (OM) and SEM images, and a spatial distribution of machining induced deposits and detailed morphology of machined trench are shown by gradually zoomed-in SEM images while detailed characteristics of redeposited nanomaterials at the machining edge (Edge) and the interline center location (Center) are compared.

By the interline separation of 200 μm, a wide region between lines is free from laser-induced deposits, and the interline center is completely void of any deposits, which is an anticipated situation from the laser affected width of ~ 50 μm observed in Fig. 3. Multi-line machining by the interline separation of 100 μm corresponds to the regime of entire processing coverage on sample surface despite a large spatial variation in redeposited nanomaterial distribution - the interline center barely starts to accumulate the deposits induced by two consecutive machining events while the overall distribution of nanomaterials is still dictated by single line machining process, i.e., dense to course distribution of nanofibrous structures from machining edge to interline center.

By the interline separation of 50 μm, improved spatial uniformity is achieved with larger amount of material deposition as expected. Overall, uniformly darker region in optical microscope image is found, but the region near the upper edge deviate from such trend identified as brighter

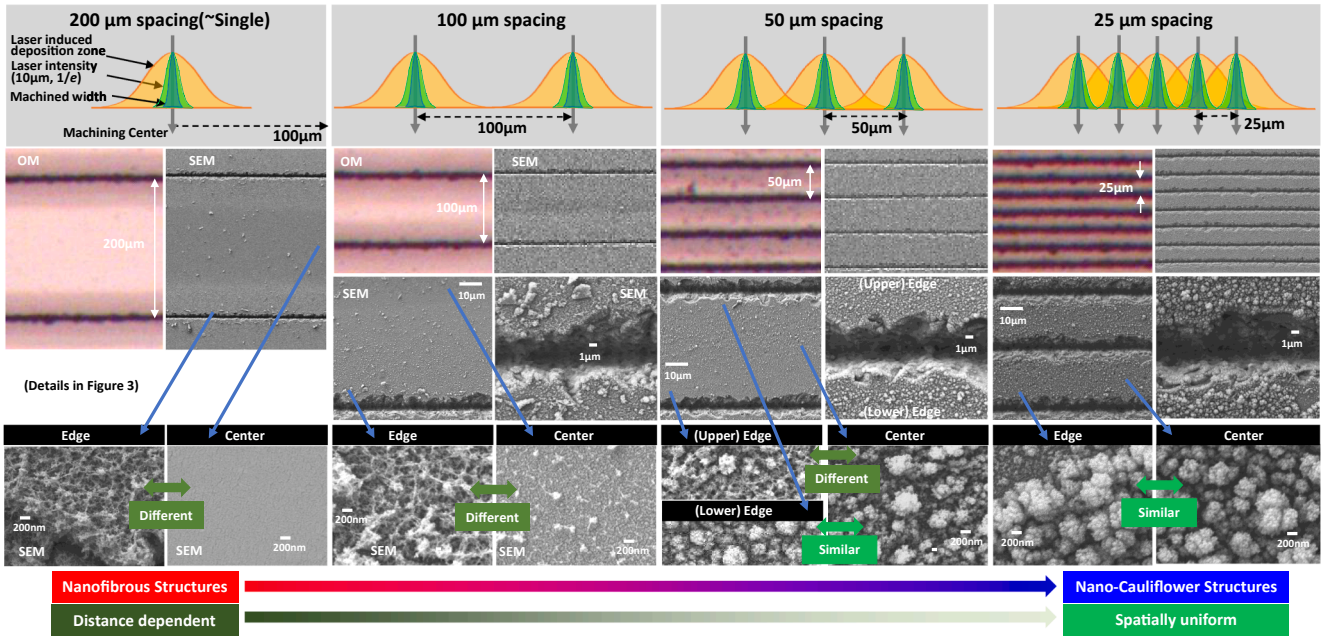

Fig. 4. Multi-line laser micromachining results on glass surface. A picosecond laser beam of ~12 ps in temporal pulse width, 532 nm in wavelength, 100 kHz in pulse frequency and 400 mW in average power was focused on the glass sample surface at ~10 μm focal spot diameter, and for unit machining line sample scan speed was fixed at 20 mm/s while separation between lines was varied; 200, 100, 50 and 25 μm. For each case of interline separation, lateral extent of machined trench (Machined width), Gaussian laser intensity profile (Laser intensity) and laser machining induced nanomaterials redeposition (Laser induced deposition zone) are schematically drawn on top portion of the figure, and overall laser-machining affected zone is also visualized experimentally by optical microscope (OM) and scanning electron microscope (SEM) images.

region. SEM imaging reveals that in the darker region covering most of interline spacing, a new particle arrangement composed of discrete spherical nanoparticle aggregates is developing with increased overall thickness while the brighter region near upper edge is still characterized as web-like nanofibrous structures with smaller film thickness. It is mentioned that the lines in the upper locations were machined ahead of lines in the lower locations in Fig. 4. Any line scan based micromachining (except the first line) with 50 μm interline separation, will remove part of materials deposited by the previous line scan near its border although additional material deposition by the next line scan will be followed. Therefore, it is reasonable that the region near upper edge has less amount of deposited materials, explaining the existence of brighter edge region with smaller thickness. Upon further reduction of interline separation to 25 μm, a higher spatial uniformity was achieved, possibly making up the discrepancy near the upper edge by increased material supply rate, and the discrete spherical aggregates ultimately developed towards nano-cauliflower structures. It is believed that such transition from nanofibrous to discrete spherical aggregates and nano-cauliflower structures is attributed to the increased amount of material source as similar material supply rate dependent structural transition was reported by gradually decreasing gas pressure in the PLD configuration based on picosecond laser of 200 kHz pulse frequency [20].

Fig. 5 shows the morphology of laser-machined samples after HF etching. As explained in Fig. 2(b), HF etching process removes loose components including redeposited nanomaterials, thus leaving robust micromachined trench structures only. After HF etching, essentially no interline separation dependent surface and trench characteristics are

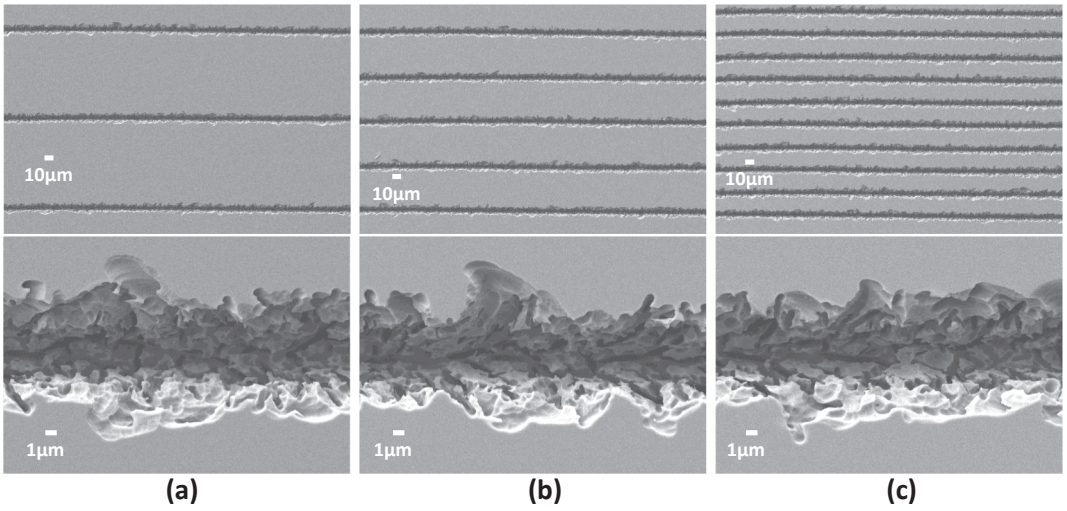

Fig. 5. Scanning electron microscope (SEM) images of laser-machined samples after HF etching. Interline separation is 100 μm in (a), 50 μm in (b) and 25 μm in (c).

found. Samples after HF will serve as reference samples in characterizing nanomaterial dependent wetting characteristics in next section.

3.3. Study on water wetting behavior in ambient air

The wetting behavior of the studied laser-patterned glass surfaces is characterized for water in ambient air using the micromachined surfaces with different interline separations of 25, 50, 100 and 200 μm. Since the main objective is to identify the role of the redeposited nanomaterials on the surface wetting properties, we characterize and compare laser-patterned glass surfaces with the deposited nanomaterial reported in Fig. 4 and the same surfaces treated with an additional HF etching step that removes the redeposited nanomaterials, as reported in Fig. 5.

It is mentioned that the configuration of Wilhelmy plate measurement is performed while maintaining machined microgrooves parallel to the water level in the course of wetting/de-wetting as schematically depicted in Fig. 6(a). Although the sessile drop based approach allows a convenient measurement of contact angles [36], anisotropic wetting occurs by a sessile drop preferentially along the direction of fabricated line patterns as previously reported by other groups [23]. The current study is rather focused on evaluating the wetting behavior across the micro line patterns relying on the configuration of Wilhelmy plate. Wilhelmy plate measurements described in Fig. 6(a) are performed with a force tensiometer (Biolin Sigma 700) and enable the determination of the tensiometer force F on the sample and its hysteretic behavior (Fig. 6 (b)–(e)) as a function of the immersion depth d as the micropatterned surfaces are immersed into and withdrawn from a water bath in ambient air. It is observed from the force–displacement curves (Fig. 6(b)–(e)) that the hysteresis between the forces measured during immersion and withdrawal is nearly completely suppressed for the micromachined surfaces that are fully covered by nanomaterial as reported in Fig. 4 for line separations smaller than 100 μm. Notably, the micromachined surfaces that are treated with HF to remove nanomaterial deposition display the same hysteresis loop independently of the line spacing employed (red curves in Fig. 6(b)–(e)).

The Wilhelmy plate method at the employed low plate speed $V = 1$ mm/min corresponding to extremely small capillary numbers $Ca \sim 10^{-7}$ can be used to determine the static advancing and receding contact angles θ_A and θ_R, respectively, by assuming that the measured tensiometer force is $F(d) = \gamma\cos\theta 2(w+h) + \rho gwhd$, where $\gamma = 72.3$ mN/m is the surface tension of the water–air interface, θ is the advancing or receding contact angle during immersion or withdrawal, w and h are the sample width and thickness, respectively, $\rho = 980$ kg/m^3 is the density of water, and g is the gravitational acceleration. The average value and uncertainty for θ_A and θ_R, and the contact angle hysteresis range θ_A - θ_R determined from the tensiometer force during 5 immersion-withdrawal cycles are reported in the table in Fig. 6(g). We note that similar static contact angles $\theta_S = (\theta_A + \theta_R)/2 \simeq 20^\circ$ are measured for both the micromachined surfaces with and without nanomaterials. However, the hysteresis range is $\theta_A - \theta_R \simeq 20 - 30^\circ$ for surfaces without nanomaterials, while $\theta_A \simeq \theta_R$ for the surfaces covered with deposited nanomaterial and the contact angle hysteresis range decreases below the measurement uncertainty (~3°) as the line separation is reduced below 100 μm. The much larger hysteresis range for the surfaces treated with HF that lack deposited nanomaterials show no correlation with the line separation. These results indicate the key role of the nanomaterial deposition in suppressing contact angle hysteresis and suggest the possible infusion of water in the course of multiple successive immersion

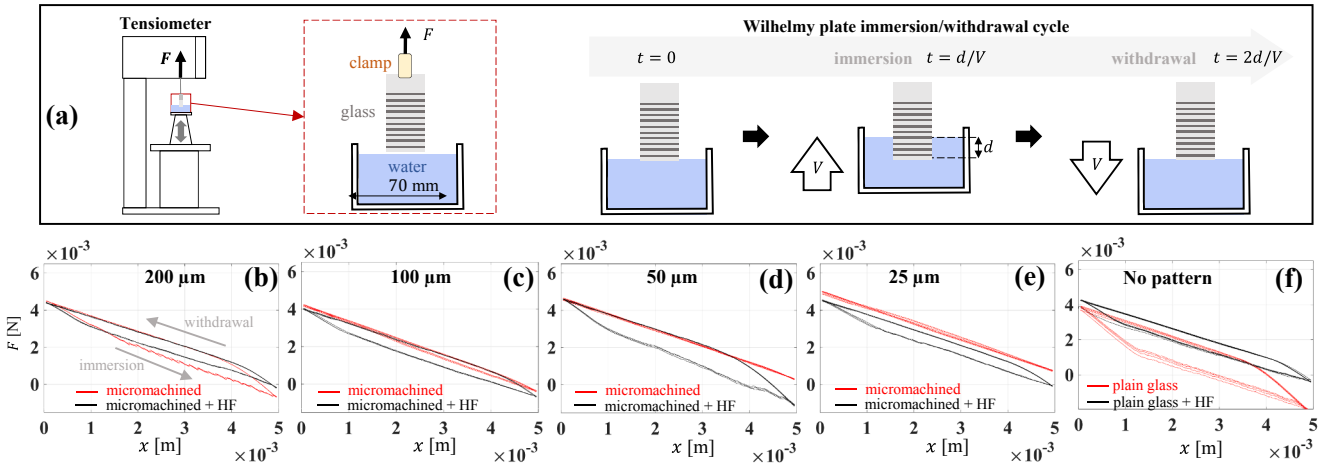

(g)

Spacing [μm]	Micromachined surfaces (nanomaterial deposition) θ_A [deg]	θ_R [deg]	$\theta_R - \theta_A$ [deg]	Micromachined surfaces + HF etching θ_A [deg]	θ_R [deg]	$\theta_R - \theta_A$ [deg]
25	20.8±2.8	19.17±3.09	1.67±0.37	30.7±0.82	12.1±2.94	18.54±2.17
50	19.04±2.78	16.14±3.7	3.05±1.05	40.2±1.53	8.81±1.79	31.42±0.95
100	29.6±2.64	22.29±3.1	7.39±0.58	36.42±1	15.2±2.35	21.21±1.4
200	40.5±1.9	12.5±0.76	28.01±2.63	29.6±1.5	6.1±3.5	23.5±2.55
No pattern	56.08±2.07	24.6±1.61	31.41±0.47	31.9±0.53	6.43±1.7	25.5±1.26

Fig. 6. Characterization of the wetting forces, contact angles, and hysteresis range for micromachined surfaces with and without nanomaterial deposition. (a) Schematic of the Wilhelmy plate (force–displacement) measurements with immersion and withdrawal cycles at a low plate speed ($V = 1$ mm/min). The micromachined surface patterns are parallel to the water–air interface. (b–e) Force-displacement curves obtained during five consecutive immersion-withdrawal cycles for the micromachined surfaces with and without HF etching and line separations from 25 to 200 μm (see legend), and (f) for plain glass surface with and without HF etching. Hysteresis loops are observed when nanomaterial deposits do not fully cover the surface. (g) Tabulated average and uncertainty (95% confidence interval) values for the advancing, θ_A, and receding, θ_R, contact angles and hysteresis range $\theta_A - \theta_R$, as determined from force-displacement measurements.

and withdrawal cycles performed during the Wilhelmy plate measurements. Treating a glass surface with HF is known to reduce the equilibrium contact angle of water but it has limitation in suppressing the contact angle hysteresis. Such trend is shown in our measurements using non-patterned glass before and after treatment with HF in Fig. 6(f). After treatment with HF the equilibrium contact angle is reduced but the difference between advancing and receding contact angles is over 20 deg. It is also noted that the influence of micropattern was minor after HF treatment.

The force–displacement measurements reported in Fig. 6 showed the repeatable wetting trend over multiple immersion/withdrawal cycles, and multiple attempts after complete sample drying, indicating that the nanomaterials were not removed from the studied samples.

We further perform optical analysis of the wetting process in the Wilhelmy plate measurements to examine whether the infusion of a lubricating water film is involved in suppressing contact angle hysteresis for the micromachined surfaces with deposited nanomaterial. Fig. 7(a) shows the progression of the static meniscus for the patterned surface with 25 μm line separation (i.e., the surface entirely covered by redeposited materials in nano-cauliflower shape reported in Fig. 4). A pre-wetting front or precursor film is observed (Fig. 7(a)) above the static meniscus during the wetting process after the plate gets in contact with the water bath. Such precursor film is not observed for the patterned surfaces with HF etching to remove nanomaterial deposits. The observation of a pre-wetting front is consistent with the hysteresis suppression reported by Wilhemy plate measurements for the micromachined surfaces covered by nanomaterials and the previously reported wicking behavior of laser-patterned glass surfaces [23]. We observe that the infused water can remain on the surface (Fig. 7(b)) for several minutes depending on the humidity of the ambient air environment. Such hysteresis free behavior is attributed to the enhanced hydrophilicity via redeposited nanomaterials, and the current experimental results are consistent with the Wenzel model [23] in that the surface texture will enhance the hydrophilicity of an originally hydrophilic surface while it will enhance the hydrophobicity of an originally hydrophobic surface. In our study, the plain glass surface is originally hydrophilic, and thus the surface patterning should enhance the hydrophilicity.

Further details of water wetting behavior are inspected by the optical microscope imaging during the wetting stage of Wilhelmy plate measurements for the patterned surfaces by 25, 50, 100 and 200 μm interline separations before and after HF etching as summarized in Fig. 8. All the microscope images were taken from a fixed height of 4 mm (at the image center) from glass sample's bottom edge in an optical transmission mode. Time elapses (t) marked in the figure were counted from the moment the rising water level just touched glass sample's bottom edge, and arrows indicate a few progressive locations of the most advancing meniscus at the early stages of wetting.

A noticeable characteristic of patterned surfaces, especially by 25 and 50 μm interline separations, is a rapid infusion of thin water layer; pre-wetting fronts reached the inspected height location of 4 mm from the sample edge almost immediately within $t < 1$ s. The patterned surface by 100 μm interline separation also showed a similar pre-wetting trend although the spatial extent of pre-wetting is limited. On the contrary, no pre-wetting front was observed on the patterned surface by 200 μm interline separation. It is mentioned that the pre-wetting fronts tend to progress in a stepwise fashion across the machined trenches, wetting each interline section one by one. The stepwise progression on patterned surfaces by 25 and 50 μm interline separations was continuous, but that on the patterned surface by 100 μm interline separation was frequently interrupted after passing each of machined trench and the upward movement of trapped bubbles assisted the stepwise progression. The pre-wetting trend is obviously attributed to the deposited nanomaterials as confirmed by comparison tests on surfaces after HF etching (right figures in Fig. 8). Essentially, the negative micro-features did not significantly affect the wetting behavior without nanomaterials.

Once the pre-wetting occurs on the patterned surfaces, the nominal meniscus of sufficient water thickness, as identified by high image contrast in the optical microscope images, should subsequently proceed over the infused surface with very low advancing contact angle, thus enabling the hysteresis free behavior. Accelerated meniscus motion on the infused surfaces is noticed on patterned surfaces by 25, 50 and 100 μm interline separations vs. surfaces without nanomaterials after HF etching (compare t's in Fig. 8). On the patterned surface by 200 μm interline separation, the stepwise wetting motion was noticeably slowed down, and the observed wetting process was composed of two alternating steps; a longitudinal wetting along each interline section assisted by hydrophilic arrangement of nanomaterials, and a meniscus jumping into next interline section. Overall, the two-step process significantly retarded the meniscus progression on the patterned sample by 200 μm interline separation, indicating that the negative micropatterns can serve as a certain type of barrier when combined with nanomaterials of a graded distribution along the vertical direction.

4. Conclusion

Glass surface micromachining was performed using a picosecond laser of visible wavelength towards simultaneous redeposition of nanomaterials in the neighborhood of machined trench. Upon machining a single discrete negative line pattern of ~10 μm width, the machined debris was redeposited in the form of web-like nanofibrous

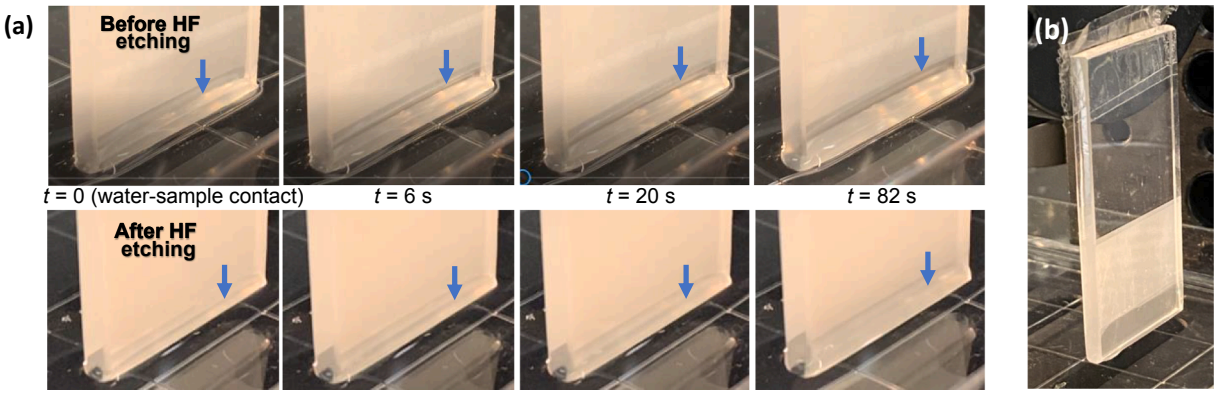

Fig. 7. Pre-wetting front observed in Wilhelmy plate configuration with 5 mm vertical immersion of the micromachined surface samples. Water level is rising at a constant velocity of 1 mm/min for wetting and moving down at the same speed for dewetting while the sample is held fixed. (a) Selected snapshots of time-resolved imaging for patterned surface by 25 μm line separation (upper images) and the surface after HF etching (lower images). The time elapse (t) is from the contact of the sample bottom edge with the water bath, and arrows indicate the progressive locations of the pre-wetting front. (b) Photograph of the as-patterned sample by 25 μm line separation after completing one wetting/dewetting cycle. Distinctive region near sample bottom edge indicates the zone with infused water.

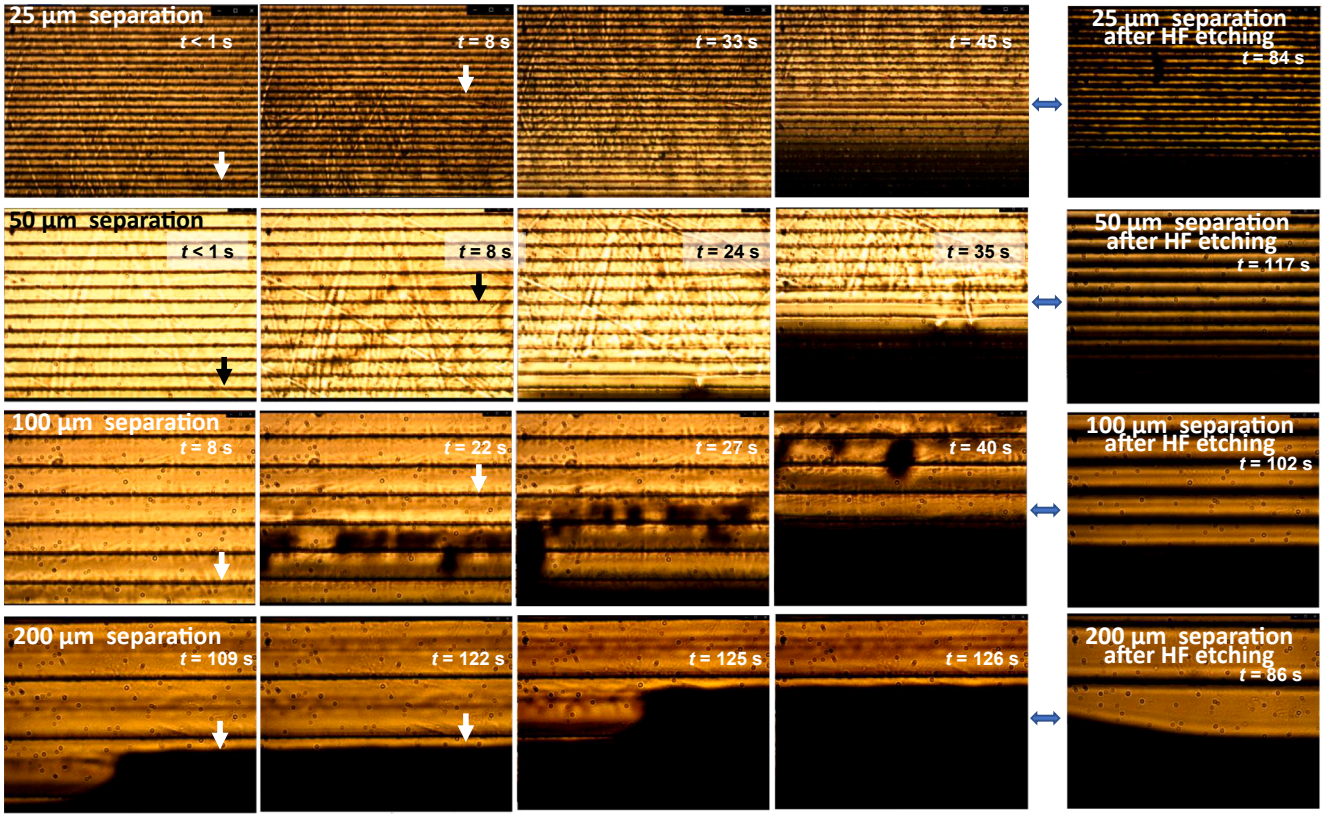

Fig. 8. Progression of water wetting visualized by optical microscope imaging during wetting stage of Wilhelmy plate measurements for the laser patterned surfaces by 25, 50, 100 and 200 μm interline separations (left 4 figures) and the surfaces after HF etching (right figures). Water level was rising at constant velocity of 1 mm/min while samples were fixed, and the optical microscope images were taken at a fixed vertical height location of 4 mm from sample's bottom edge. Time elapse (t) was counted from the moment the rising water level touched sample's bottom edge, and arrows indicate the progressive locations of the most advancing meniscus.

aggregates, possibly assembled from suspended nanoparticles in ambient air, and the lateral extent of redeposition was around 50 μm in both direction from machining center.

Subsequently multi-line patterning was performed by different interline separations towards coverage of enlarged sample area with controllable nanomaterials arrangement. As anticipated from single line characteristics, gradual reduction of line distance from 200 to 100 μm allowed nanomaterial coating over the entire interline spacing with varying number density while maintaining similar web-like nanofibrous structures. Line distances of 50 and 25 μm significantly improved the spatial uniformity but web-like nanofibrous characteristics were converted to nano-cauliflower structures based on supply of larger amount of redeposited materials. In this way, picosecond laser machining process enabled a single-step fabrication of multi-hierarchical micro/nano structures on arbitrary glass surface area with controllable nanomaterial characteristics.

The wetting behavior of the patterned surfaces by water was also examined in ambient air comparing surfaces with different interline separations with and without nanomaterial deposition. Force-displacement measurements report that the deposition of nanomaterials has the effect on suppressing the contact angle hysteresis and associated wetting forces leading to adhesion of water droplets and/or solid particles. The nearly complete suppression of the contact angle hysteresis is attributed to the infusion of water in the complex porous networks formed by the deposited nanomaterials, as further corroborated by optical imaging. We thus report that the employed laser fabrication method can efficiently produce so-called slippery liquid-infused porous surfaces (SLIPS) with superhydrophilic behavior possibly enabling anti-icing and self-cleaning or antifouling properties [2,3,37]. Moreover, the employed laser patterning method can simultaneously produce nanoscale porous networks with controllable structural characteristics and microgrooves with complex shape. This fabrication capability can enable the design and fabrication of SLIPS with geometric designs that prevent failure under shear [38–40].

Although the current configuration of nanofeatures has maintained consistent wetting characteristics over multiple wetting/de-wetting cycles and multiple attempts after complete drying each time, next steps to improve adhesion of nanofeatures on the sample surfaces are under examination, for instance, via post-annealing steps in furnaces or hot plates towards extended lifetime in ultimate devices. Further studies on the nanomaterial deposition by a wider range of laser processing parameters (e.g., power, pulse energy, focal spot size and overlap) and the impact on the water wetting are also under way in conjunction with fundamental investigation of ablation plume dynamics as material sources.

CRediT authorship contribution statement

Zhen Wang: Investigation, Methodology, Validation, Writing - original draft. **Dhiraj Nandyala:** Investigation, Methodology, Validation, Formal analysis. **Carlos Colosqui:** Conceptualization, Writing - review & editing, Supervision. **Thomas Cubaud:** Conceptualization, Methodology, Supervision. **David Hwang:** Conceptualization, Investigation, Writing - review & editing, Supervision.

Declaration of Competing Interest

The authors declare that they have no known competing financial interests or personal relationships that could have appeared to influence the work reported in this paper.

Acknowledgement

This work was supported by the National Science Foundation through award CBET-1605809. This work used resources of the Center for Functional Nanomaterials, which is a U.S. DOE Office of Science Facility, at Brookhaven National Laboratory under Contract No. DE-SC0012704.

References

[1] D. Quere, Wetting and roughness, Annu. Rev. Mater. Res. 38 (2008) 71–99.
[2] P. Kim, et al., Liquid-Infused Nanostructured Surfaces with Extreme Anti-Ice and Anti-Frost Performance, Acs Nano 6 (8) (2012) 6569–6577.
[3] Epstein, A.K., et al., Liquid-infused structured surfaces with exceptional anti-biofouling performance. Proceedings of the National Academy of Sciences of the United States of America, 2012. 109(33): p. 13182-13187.
[4] D. Psaltis, S.R. Quake, C.H. Yang, Developing optofluidic technology through the fusion of microfluidics and optics, Nature 442 (7101) (2006) 381–386.
[5] C. Monat, P. Domachuk, B.J. Eggleton, Integrated optofluidics: A new river of light, Nat. Photonics 1 (2) (2007) 106–114.
[6] F. Kotz, et al., Three-dimensional printing of transparent fused silica glass, Nature 544 (7650) (2017) 337–339.
[7] S. Copar, et al., Microfluidic control over topological states in channel-confined nematic flows. Nature, Communications 11 (1) (2020), 59.
[8] T. Mouterde, et al., Antifogging abilities of model nanotextures, Nat. Mater. 16 (6) (2017) 658–663.
[9] A. Checco, A. Rahman, C.T. Black, Robust Superhydrophobicity in Large-Area Nanostructured Surfaces Defined by Block-Copolymer Self Assembly, Adv. Mater. 26 (6) (2014) 886–891.
[10] D. Ebert, B. Bhushan, Transparent, Superhydrophobic, and Wear-Resistant Coatings on Glass and Polymer Substrates Using SiO2, ZnO, and ITO Nanoparticles, Langmuir 28 (31) (2012) 11391–11399.
[11] J.Y. Cheng, et al., Crack-free direct-writing on glass using a low-power UV laser in the manufacture of a microfluidic chip, J. Micromech. Microeng. 15 (6) (2005) 1147–1156.
[12] K. Sugioka, Y. Cheng, Femtosecond laser processing for optofluidic fabrication, Lab Chip 12 (19) (2012) 3576–3589.
[13] M.S. Giridhar, et al., Femtosecond pulsed laser micromachining of glass substrates with application to microfluidic devices, Appl. Opt. 43 (23) (2004) 4584–4589.
[14] K. Sugioka, Y. Cheng, Ultrafast lasers-reliable tools for advanced materials processing, Light-Sci. Appl. 3 (2014), e149.
[15] J.T. Han, et al., Transparent, Conductive, and Superhydrophobic Films from Stabilized Carbon Nanotube/Silane Sol Mixture Solution, Advanced Materials 20 (19) (2008) 3724–3727.
[16] U.P. Shaik, et al., Growth of superhydrophobic Zinc oxide nanowire thin films, Mater. Lett. 75 (2012) 51–53.
[17] H.B. Zeng, et al., Nanomaterials via Laser Ablation/Irradiation in Liquid: A Review, Adv. Funct. Mater. 22 (7) (2012) 1333–1353.
[18] K. Hiromatsu, D.J. Hwang, C.P. Grigoropoulos, Active glass nanoparticles by ultrafast laser pulses, Micro Nano Lett. 3 (4) (2008) 121–124.
[19] K.T. Kang, et al., Investigation of Elemental Composition Change by Laser Ablation of a Rare-Earth Containing Material, Phys. Status Solidi a-Appl. Mater. Sci. 215 (20) (2018).
[20] M. Pervolaraki, et al., Si nanostructures grown by picosecond high repetition rate pulsed laser deposition, Appl. Surf. Sci. 278 (2013) 67–70.
[21] S. Moradi, et al., Femtosecond laser irradiation of metallic surfaces: effects of laser parameters on superhydrophobicity, Nanotechnology 24 (41) (2013).
[22] M.S. Ahsan, et al., Formation of superhydrophobic soda-lime glass surface using femtosecond laser pulses, Appl. Surf. Sci. 265 (2013) 784–789.
[23] A.Y. Vorobyev, C.L. Guo, Water sprints uphill on glass, J. Appl. Phys. 108 (12) (2010).
[24] T.L. Chang, et al., Effect of ultra-fast laser texturing on surface wettability of microfluidic channels, Microelectron. Eng. 98 (2012) 684–688.
[25] T.L. Chang, et al., Ultrafast laser ablation of soda-lime glass for fabricating microfluidic pillar array channels, Microelectron. Eng. 158 (2016) 95–101.
[26] B. Tan, K. Venkatakrishnan, Synthesis of fibrous nanoparticle aggregates by femtosecond laser ablation in air, Opt. Exp. 17 (2) (2009) 1064–1069.
[27] D. Vipparty, B. Tan, K. Venkatakrishnan, Nanostructures synthesis by femtosecond laser ablation of glasses, J. Appl. Phys. 112 (7) (2012).
[28] J.M. Liu, Simple Technique for Measurements of Pulsed Gaussian-Beam Spot Sizes, Opt. Lett. 7 (5) (1982) 196–198.
[29] C. Hnatovsky, et al., Polarization-selective etching in femtosecond laser-assisted microfluidic channel fabrication in fused silica, Opt. Lett. 30 (14) (2005) 1867–1869.
[30] M. Kim, et al., Single cell detection using a glass-based optofluidic device fabricated by femtosecond laser pulses, Lab Chip 9 (2) (2009) 311–318.
[31] J. Soderlund, et al., Lognormal size distributions in particle growth processes without coagulation, Phys. Rev. Lett. 80 (11) (1998) 2386–2388.
[32] D.J. Hwang, et al., Optical near-field ablation-induced plasma characteristics, Appl. Phys. Lett. 89 (25) (2006), 254101.
[33] D.J. Hwang, et al., Femtosecond laser ablation induced plasma characteristics from submicron craters in thin metal film, Appl. Phys. Lett. 91 (25) (2007), 251118.
[34] B.R. Tull, et al., Formation of silicon nanoparticles and web-like aggregates by femtosecond laser ablation in a background gas, Appl. Phys. a-Mater. Sci. Process. 83 (3) (2006) 341–346.
[35] M. Wilkinson, B. Mehlig, Caustics in turbulent aerosols, Europhys. Lette. 71 (2) (2005) 186–192.
[36] D. Nandyala, et al., Design, Fabrication, and Analysis of a Capillary Diode for Potential Application in Water-Oil Separation, Acs Appl. Mater. Interf. 12 (41) (2020) 45950–45960.
[37] L.L. Xiao, et al., Slippery Liquid-Infused Porous Surfaces Showing Marine Antibiofouling Properties, Acs Appl. Mater. Interf. 5 (20) (2013) 10074–10080.
[38] J.S. Wexler, I. Jacobi, H.A. Stone, Shear-Driven Failure of Liquid-Infused Surfaces, Phys. Rev. Lett. 114 (16) (2015).
[39] C.E. Colosqui, et al., Crossover from shear-driven to thermally activated drainage of liquid-infused microscale capillaries, Phys. Rev. Fluids 1 (6) (2016).
[40] M. Villegas, et al., Liquid-Infused Surfaces: A Review of Theory, Design, and Applications, Acs Nano 13 (8) (2019) 8517–8536.